Ablation by short optical and X-ray laser pulses

N.A. Inogamov[a], S.I. Anisimov[a], V.V. Zhakhovsky[b,c], A.Ya. Faenov[b,d], Yu.V. Petrov[a],
V.A. Khokhlov[a], V.E. Fortov[b], M.B. Agranat[b], S.I. Ashitkov[b], P.S. Komarov[b], I.Yu. Skobelev[b],
Y. Kato[e], T.A. Pikuz[b,d], V.V. Shepelev[f], Y. Fukuda[d], M. Tanaka[d], M. Kishimoto[d], M. Ishino[d],
M. Nishikino[d], M. Kando[d], T. Kawachi[d], M. Nagasono[g], H. Ohashi[g,h], M. Yabashi[g,h], K. Tono[g]
, Y. Senda[h], T. Togashi[g,h], and T. Ishikawa[g]

[a]Landau Institute for Theoretical Physics, Russian Academy of Sciences, Chernogolovka
142432, Russia;
[b]Joint Institute for High Temperatures, Russian Academy of Sciences, Moscow 125412, Russia;
[c]Department of Physics, University of South Florida, Tampa, Florida 33620, USA;
[d]Kansai Photon Science Institute, Japan Atomic Energy Agency, Kyoto 619-0215, Japan;
[e]The Graduate School for the Creation of New Photonics Industries, Hamamatsu, Shizuoka
431-1202, Japan;
[f]Institute for Computer Aided Design, Russian Academy of Sciences, Moscow, 123056, Russia;
[g]XFEL RIKEN, SPring-8, Hyogo 679-5198, Japan;
[h]Japan Synchrotron Radiation Research Institute, SPring-8, Hyogo 679-5198, Japan

ABSTRACT

The paper is devoted to experimental and theoretical studies of ablation of condensed matter by optical (OL),
extreme ultraviolet (EUV) and X-ray lasers (XRL). Results obtained at two different XRL are compared. The
first XRL is collision Ag-plasma laser with pulse duration $\tau_L = 7$ ps and energy of quanta $h\nu$=89.3 eV, while
the second one is EUV free electron laser (EUV-FEL) and has parameters $\tau_L = 0.3$ ps and energy of quanta 20.2
eV. It is shown that ablation thresholds for these XRL at LiF dielectric are approximately the same. A theory is
presented which explains slow growth of ablated mass with fluence in case of XRL as a result of transition from
spallative ablation near threshold to evaporative ablation at high fluencies. It is found that the metal irradiated
by short pulse of OL remains in elastic state even in high shear stresses. Material strength of aluminum at very
high deformation rates $\dot{V}/V \sim 10^9$ s^{-1} is defined.

Keywords: Short pulse laser ablation, EUV and X-ray laser ablation of LiF, material strength defined in laser
experiment

1. INTRODUCTION

Short pulse OL and XRL are important for practical applications. Ablation by these lasers is used for micro fab-
rication treatment of surfaces of metals, semiconductors, and dielectrics. The paper presents results of three sets
of experiments together with their physical modeling and computer simulation. The first two sets are obtained at
two very different XRL (different τ_L, $h\nu$) but results concerning *low value of ablation threshold* are similar. Low
value means high efficiency of short pulse XRL in comparison with nanosecond XRL or in comparison with fs, ns
OL. This similarity between the two XRL is due to the short durations τ_L of both XRL. They are shorter than,
or comparable with acoustic time $t_s = D_{att}/c_s$ which is necessary for sound to travel with speed c_s through an
attenuation depth D_{att}. In this sense such short pulses may be called "supersonic". These "supersonic" pulses
create thermomechanical stresses which are the reason for spallative ablation. Thermomechanics and negative
pressure define character of ablation at relatively low fluencies of the order of ablation threshold. At such flu-
encies, heating is moderate and matter remains in condensed state where cohesive properties are dynamically

important. At higher fluencies, XRL transfers the first heated layer with thickness D_{att} into gaseous state where cohesion is not significant.

The third set of experiments is performed at Ti:sapphire OL. Aluminum (Al) films deposited on glass plate are irradiated by short pulse. Pump-probe technique of excitation and measurements is used. Pump pulse arrives through a glass plate and heats Al near a glass/Al contact. Probe pulses reflect from a rear side of the Al film. By measuring the phase of a reflected probe light wave as function of delay time between pump and probe, we obtain information about motion of the rear side surface of the Al film. This information is compared with two-temperature physical model. The comparison allows to obtain data about formation and propagation of powerful acoustic disturbances created thermomechanically by absorption of short OL pulse. These data, firstly, shed light on a state in which shock wave transfers metal, and, secondly, allow to determine material strength at impulsive load.

Two physical models are developed for description of XRL/dielectrics and OL/metals cases. Laser pulse is absorbed by electronic subsystem of condensed matter. The rate of energy exchange $\dot{E}_{ei}$ between electron and ion subsystems is limited since ions are much more massive than electrons. For short pulses, the energy exchange time t_{eq} exceeds pulse duration τ_L. In this case the two-temperature situation $T_e \gg T_i$ appears. Electrons are hotter and transfer the excess of their energy to ions: therefore T_e decreases while T_i increases - the temperature difference becomes smaller and smaller. Temperature relaxation to equilibrium $T_e = T_i$ takes time $\sim t_{eq}$.

Considered fluencies are such that the heating of the first heated layer with thickness D_{att} corresponds to the thermodynamical state between the triple and the critical points. Density during heating is of the order of solid state density and internal energy per atom is in kiloKelvin-few eV range. This is the warm dense matter (WDM) range. Short pulse OL and XRL transfer matter first into two-temperature WDM state. Usual one-temperature WDM appears with delay of the order of $\sim t_{eq}$. The two-temperature stage is an important part of the whole process.

There is qualitative difference between the two-temperature dielectrics and metals. In metals, conduction electrons are already present while in dielectrics they appear as the result of photo and impact ionization from valent band. The ionization degree $Z = n_e/n_p$ is in the 1-100% range for widegap dielectric LiF in our range of energies from fluencies near ablation threshold $F_{abl} \approx 10$ mJ/cm^2 and up to fluencies $F \sim 20F_{abl}$, here n_e, n_p are concentration of free electrons in a conduction band and concentration of pairs of Li and F atoms, $n_p = 6 \cdot 10^{22}$ cm^{-3} at room temperature. A difficult and important problem concerning value of an electron-ion energy exchange rate $\dot{E}_{ei} = \alpha(T_e - T_i)$ for dielectrics is solved in this paper. The coefficient α has remained unknown for dielectrics. Our calculations show that $\alpha \to 0$ when $Z \to 0$ and that α_{LiF} is 1.7-2 times higher than α_{Al} for aluminum at typical ionization degrees $Z \sim 0.1 - 1$ of LiF. This is a consequence of small mass of Li atom and ionic character of LiF crystal.

2. X-RAY EXPERIMENTS

The experiment with the first XRL facility has been performed at Kansai Photon Science Institute (KPSI) of Japan Atomic Energy Agency (JAEA). The Ag XRL ($\lambda = 13.9$ nm) has been significantly upgraded in comparison with our previous investigations,[1,2] when a single target was employed. In the new experiments the oscillator-amplifier configuration was used.[3,4] This configuration allows to generate a completely coherent XRL beam. The XRL pulse had an average energy ~ 300 nJ and pulse duration $\tau_L = 7$ ps. The Ag XRL worked in 0.1 Hz regime and had the horizontal and vertical angular divergences at FWHM equal to 1.2 mrad x 0.4 mrad, respectively.

The XRL beam was focused on a LiF crystal of 2 mm thickness and 20 mm diameter. To focus a beam we used a spherical Mo/Si multilayer mirror of 1050 mm radius of curvature. The x-ray mirror was placed at a distance of 2715 mm from the XRL output and was used at the incidence angle of 2°. The LiF crystal was moved along the propagation direction of the XRL beam and also, after each shot, the crystal was moved in the direction perpendicular to the propagation direction. This is necessary for recording of the beam patterns at different focusing distances (motion along propagation) and on the fresh LiF crystal surface (shifts perpendicular to propagation). A 0.2 micron thick Zr filter was settled in front of the X-ray mirror at the distance 800 mm from the XRL exit in order to reduce the scattered optical radiation and the thermal X-ray emission from the

plasma produced by ps optical laser. The transmittance of the Zr filter was $\approx 49\%$ and the reflectivity of the Mo/Si mirror was $\approx 50\%$, both at 13.9 nm. Therefore, the total energy of the XRL pulse at the LiF crystal was ≈ 75 nJ in each shot.

The experiment with the self-amplified spontaneous-emission free electron laser (SASE-FEL) facility has been performed at the SPring-8 Compact SASE Source (SCSS). It can provide laser pulses in the extreme-ultraviolet (EUV) region (51-62 nm).[5–7] In our experiments SCSS worked at wavelengths about 61.5 nm. We have used a single shot mode, which allows to measure the laser energy in each shot.[7] SCSS pulse energy have been varied from 4 to 11 μJ in different shots. The duration of the pulse was about 300 fs.[6]

The Kirkpatrick-Baez microscope, based on ellipsoidal and cylindrical mirrors coated by SiC multilayers was used to focus EUV beam at the distance about 100 cm from the mirror output. The transmission of the microscope is $\sim 70\%$. The LiF crystal has been shifted along the FEL beam propagation direction and also after each shot perpendicular to it. This has been done as in the experiments with Ag XRL for recording of the beam patterns at different focusing distances on the fresh LiF crystal surface. To find the ablation threshold of LiF crystals, we varied EUV-FEL energy and/or change a focusing position from the best focus at the surface of a LiF crystal to defocusing from the best focus up to 40 mm.

The luminescence of stable color centers (CCs)[8–10] formed by XRL radiation, was used to measure the intensity/fluence distribution in the Ag XRL and SCSS laser focal spots.[11] This is very important as this allows us to define accurate value of real local fluence at a target surface. This improvement (with marking of the intensity distribution by the CCs) allows to find exact values of the ablation threshold. This is significant since, due to strong abberations, the intensity distribution has complicated and smeared-out shape and near threshold F_{abl} only small part (10-30%) of pulse energy is inside the ablation crater.

The photo-luminescence patterns from the color centers (CCs) in LiF (after irradiation of the LiF crystal with the X-ray laser beam) were observed by using a confocal fluorescence laser microscope (OLYMPUS model FV300). An 488 nm Ar laser has been used in the microscope to excite CCs, which then emit luminescence light in the spectral range 500-800 nm with the peaks at 530 nm for F2 CCs and 670 nm for F3+ CCs, respectively. To confirm that the surface of crystal has been damaged, we used an OLYMPUS BX60 microscope in visible and differential modes. Also, cross sections of the ablated craters were measured with an atomic force microscope (AFM, TOPOMETRIX Explorer) operating in the tapping mode. Typical images of the Ag XRL and SCSS laser beams, recorded with the LiF crystal at different focusing positions, are presented in Figures 1a and 1b.

Two types of experimental investigations of X-ray coherent beam radiation threshold of LiF crystals were done. In the first set of experiments with Ag XRL, we repeated our previous measurements[1,2] of LiF ablation by 7 ps laser pulse, but now more divergent and coherent beam was produced by using oscillator-amplifier configuration scheme working with 0.1 Hz repetition rate.[12,13] Despite the fact that total laser energy in our new experiments was lower in comparison with previous experiments, we obtained more stable LiF ablation due to better quality of the focusing mirror. For measurements of ablation threshold for LiF crystal, we varied focusing position of the XRL beam to reduce the beam intensity. Typical images in luminescence and differential visible modes are presented in Fig. 1a. As it is obviously seen from this Figure, our new experimental results have confirmed the results obtained previously. Again, we have obtained low value for the ablation threshold $F_{abl} \approx 10 \text{mJ/cm}^2$. As had been said above, this value is much lower than thresholds for ns XRL and for fs, ns OL.

The second type of experiments was performed by using 61.5 nm SCSS free electron laser facility. The SCSS beam allows to measure laser beam energy in each shot, and to obtain damage on LiF crystals in large areas and in much wider range of laser fluencies. This is important advantages of the SCSS device in comparison with the Ag XRL described above. As it can be seen from Figs. 1b, 2, and 3, damages on the surface of LiF crystals, due to the action of SCSS beam, were observed not only in the case of placing of a LiF crystal in the best focusing position, but also even in the case when crystal was 26 mm out of focus. In the later case, the size of ablation zone had reached a very large value $\sim 0.035 \text{mm}^2$. Large defocusing of the EUV-FEL beam and irradiation of target by pulses with different EUV-FEL intensities permitted, essentially, to vary laser flux and to measure the LiF ablation threshold accurate enough. From Figure 1b we can see that fluence $\sim 7.1 \text{mJ/cm}^2$ is not sufficient yet for EUV-FEL production of ablation on the surface of LiF crystal. Meanwhile, fluence $\sim 9.2 \text{mJ/cm}^2$ was sufficient to produce clear spot on the surface of the LiF crystal.
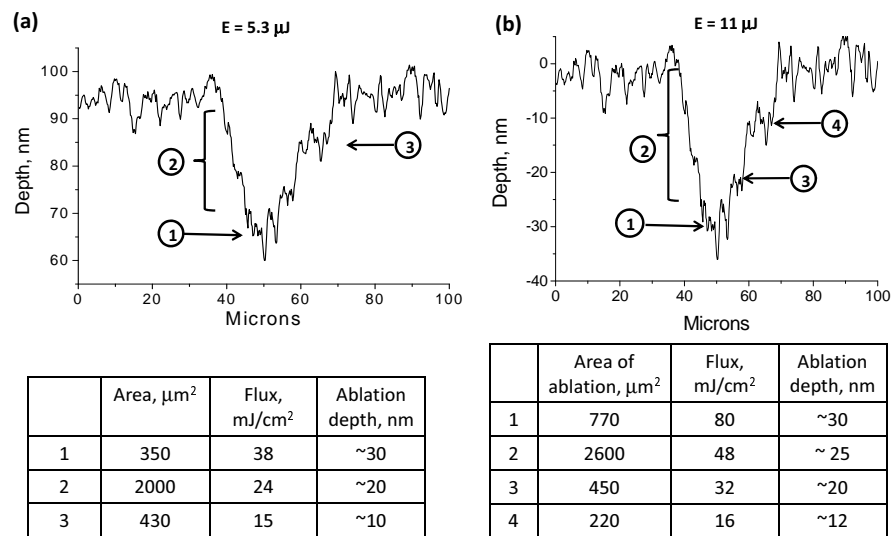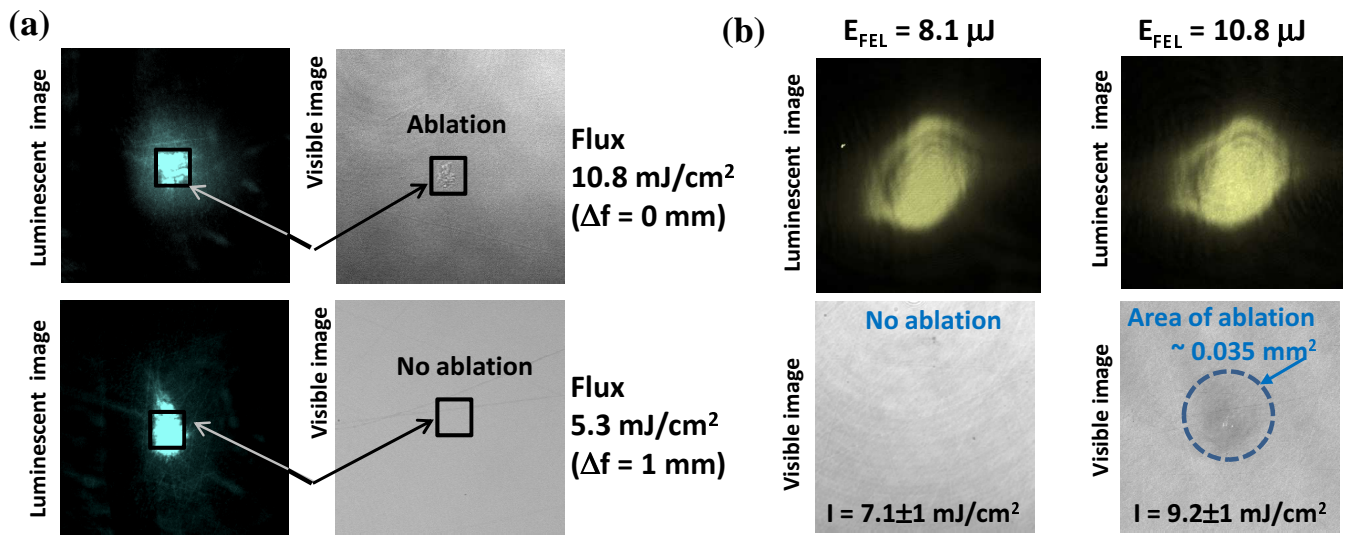
Figure 1. a) The patterns of the Ag XRL irradiation recorded on LiF crystal. The crystal is placed in the best focusing position and 1 mm out of it. b) The patterns irradiated by EUV-FEL and recorded on LiF crystal, placed in the best focusing position and 26 mm out of it. Images were obtained by Olympus microscope working at luminescent and visible modes. The area of ablation is marked on the visible images.

	Area, μm^2	Flux, mJ/cm^2	Ablation depth, nm
1	350	38	~30
2	2000	24	~20
3	430	15	~10

	Area of ablation, μm^2	Flux, mJ/cm^2	Ablation depth, nm
1	770	80	~30
2	2600	48	~ 25
3	450	32	~20
4	220	16	~12

Figure 2. a,b) Traces from AFM images of patterns recorded on LiF crystal placed 5 mm apart from the best focusing position. Crystal was illuminated by EUV-FEL beam with energy 5.3 or 10.8 μJ. Traces show that different ablation zones could be selected, which correspond to laser fluences from 16 to 80 mJ/cm^2. These different zones are marked by digits 1,2,3 (for pulse energy 5.3 μJ) or 1-4 (10.8 μJ). The corresponding ablated depths for them are listed in Tables. Small change of an ablation depth from $\approx$ 12nm to $\approx$ 30nm with significant increasing of laser fluence has been observed.
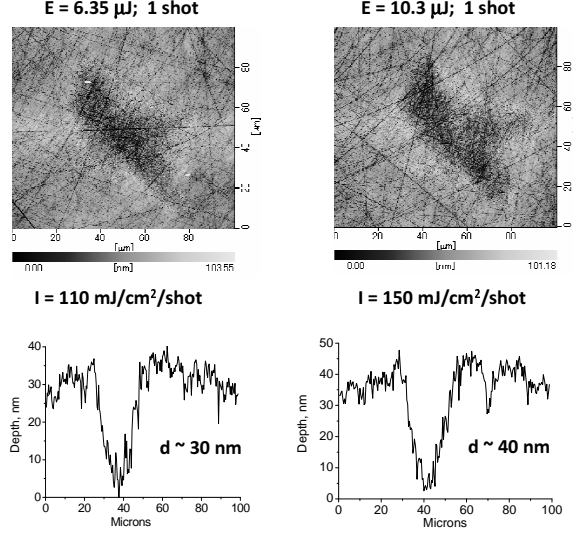
Figure 3. AFM images of patterns recorded on LiF crystal placed at the best focusing position. Crystal was illuminated by 1 shot of EUV-FEL beam with different energies. Traces of presented images clearly demonstrate that LiF crystal ablation depth increases very slowly with increasing of laser fluence.

It is also very interesting to compare the changes of ablation depth in different ablation zones, which were irradiated by EUV-FEL with different fluencies. We have determined that the smallest depth, which appears near ablation threshold of LiF crystal, is 10-15 nm (see Fig. 2). Meanwhile, increasing laser fluence up to 80 mJ/cm² does not efficiently increase the ablation depth, which reaches the value of only about 30-35 nm. This result is different enough in comparison with irradiation of LiF crystals by 7 ps Ag XRL laser where we observed the depths of ablation about 40-50 nm near the ablation threshold. Fig. 3 presents the results obtained by irradiation of LiF crystals at even greater intensities, proving the slow increase of ablation depth with increasing of EUV-FEL fluence. From Fig. 3 it is clear that even under irradiation of EUV-FEL fluences about 110 -150 mJ/cm² the ablation depth is quite small and varied around 30-40 nm.

3. MAIN EQUATIONS IN CASE OF XRL

In case of XRL and dielectrics following system is used

$$n_p \frac{\partial Z}{\partial t} = \frac{I}{\hbar \omega_L \, D_{att}} + \nu_{imp} n_e - \kappa_{rec} n_e^3, \tag{1}$$

$$\rho^0 \frac{\partial (E_e/\rho)}{\partial t} = \frac{\rho^0}{\rho} \frac{I}{D_{att}} - n_p^0 \Delta \frac{\partial Z}{\partial t} - \frac{\rho^0}{\rho} \alpha (T_e - T_i) - p_e \frac{\partial u}{\partial x^0}, \tag{2}$$

$$\rho^0 \frac{\partial (E_i/\rho)}{\partial t} = \frac{\rho^0}{\rho} \alpha (T_e - T_i) - p_i \frac{\partial u}{\partial x^0}, \tag{3}$$

$$\rho^0 \frac{\partial u}{\partial t} = -\frac{\partial p}{\partial x^0}, \tag{4}$$

$$\rho(x^0, t) \frac{\partial x(x^0, t)}{\partial x^0} = \rho^0, \tag{5}$$

$$\frac{\partial x(x^0, t)}{\partial t} = u(x^0, t). \tag{6}$$

Equations (1-3) define ionization degree $Z = n_e/n_p$ (1) and energies of electron (2) and ion (3) subsystems. The mathematical code corresponding to the system (1-6) is called n_e, T_e, T_i-hd, where "hd" means "hydrodynamics", and T_e, T_i are temperatures of subsystem.

Equations (1-3) are solved together with hydrodynamical equations (4-6). Lagrangian variable x^0 is linked to moving substance. The variable x^0 is the initial position of material particle. The x gives direction normal to the irradiated surface. One dimensional approach is valid since radial size of focal spot is large in comparison with attenuation depth $D_{att}(h\nu = 20.2\text{eV}) = 9\text{nm}$.[14] Physical model n_e, T_e, T_i-hd (1-6) including ionizaion kinetics (1) differs from two-temperature model 2T-hd where differential equation for ionization degree Z is absent. Model 2T-hd has been used in[15] for description of OL/metal case.

Equation (1) describes variation of concentration of free electrons n_e in moving material particle x^0 under action of XRL photo-ionization, impact ionization, and recombination. At our time intervals contributions of photo-recombination and ambipolar diffusion are small. Diffusion is weak as result of large mass of holes from narrow valent band. Therefore we neglect diffusion in equation (1) and neglect electron heat conduction in equation (2). Phonon heat conduction is small. Laser flux $I[\text{W/cm}^2]$ defines energy production per unit of volume $\partial I/\partial x = -I/D_{att}$ in equation (2). Volume energy absorption and energy of photon $h\nu$ absorbed at one-photon transition of electron from valent to conduction band give volume rate of production of free electrons in ionization equation (1).

Energy flux in (1,2) is

$$I(x^0, t) = \frac{F}{\sqrt{\pi}\tau_L} \exp\left(-\frac{t^2}{\tau_L^2}\right) \exp\left(-\frac{x^0}{D_{att}}\right). \tag{7}$$

In (7) value F [mJ/cm^2] is XRL fluence absorbed by dielectrics. Thickness of the LiF disk is 2 mm, see Section 2. This is a thick layer 2 mm $\gg D_{att} \approx 9$nm and incident fluence is totally absorbed in a surface layer (no transmission, no reflection). Initially absorbing dielectric is placed at the right semiaxis $x > 0$. Time is measured from the maximum of a laser pulse (7). Computer simulation starts from a distant wing of Gaussian function (7) at the instant $t_{start} = -5\tau_L$.

Energy budget (2) is written first for total electron energy $E_{sum} = n_e\Delta + E_e$, where $n_e\Delta$ is potential energy and E_e is kinetic energy of free electrons, $\Delta = 14$eV is an energy gap for widegap dielectric LiF. Equation (2) for kinetic energy E_e appears after presenting of potential energy as $n_e\Delta/\rho = Z(n_p^0/\rho^0)\Delta$ and differentiation ∂t. Kinetic energy E_e includes energy of quantum oscillations. Approximate expression is

$$E_e(T_e, \rho, Z) = \frac{1}{2}n_e\sqrt{(\frac{6}{5}E_F)^2 + (3k_B T_e)^2}. \tag{8}$$

In (8) the value $E_F = (3\pi^2)^{2/3}\hbar^2 n_e^{2/3}/2m_e$ is Fermi energy.[16] Pressure of free electrons is

$$p_e = (2/3)E_e. \tag{9}$$

Adiabatic expansion works for electron and ion subsystems (2), (3) are $p_e\partial u/\partial x^0$ and $p_i\partial u/\partial x^0$. Changes of momentum in dynamical equation (4) is defined by gradient of total pressure $p = p_e + p_i$.

4. EQUATION OF STATE AND IONIZATION RATE

There are three "components" which are necessary to integrate numerically the system described in previous Section 3. They are: equation of state (EOS), frequency of ionization by impact of free electron ν_{imp}, and electron-ion energy transfer coefficient α. Let us begin here with EOS for LiF. We present ionic EOS as $E_i(T_i, \rho)$, $p_i(T_i, \rho)$. Electronic excitations are included in Fermi approximation (8). From comparison of EOS for LiF and aluminum (Al) given in work[17] it follows that their EOS are very similar. In Figs. 4 and 5 their cold curves and Hugoniot shock adiabats are compared. Therefore we use wide-range EOS of Al from[17, 18] for computer simulation of XRL/LiF problem.

Frequency of impact ionization ν_{imp} in equation (1) is taken as in paper[2] from work.[21] Three-body recombination coefficient κ_{rec} is defined from detailed equilibrium.[21]
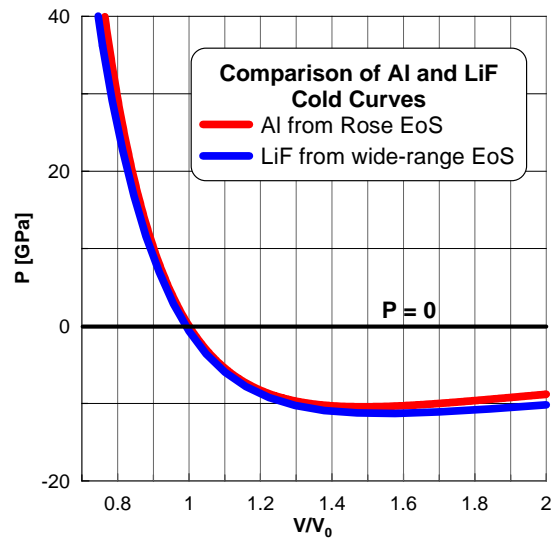
Figure 4. Cold curves called also "zero" isotherms $p(\rho, T = 0)$ or "zero" adiabatic curves $p(\rho, s = 0)$ for LiF[17] and Al,[19].[20]
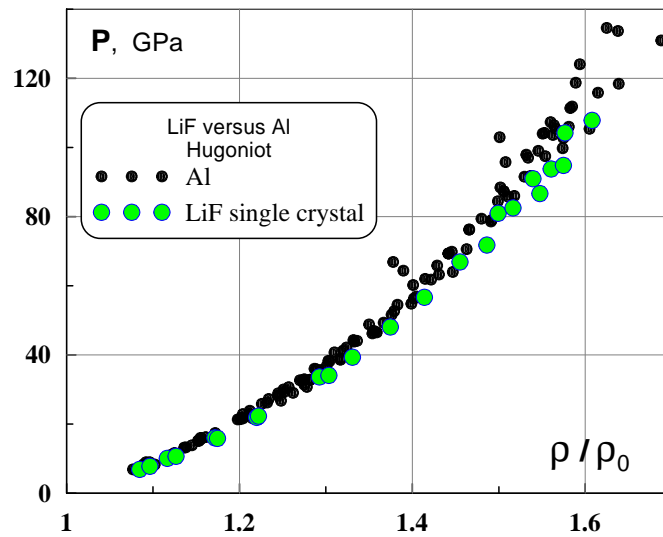

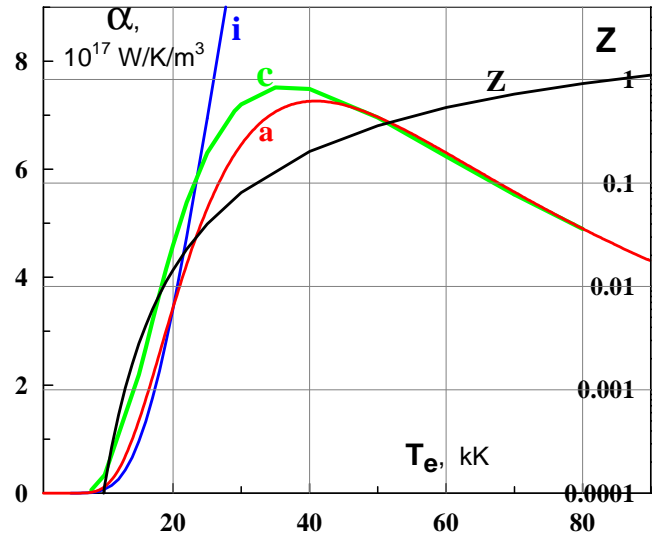Figure 5. Shock adiabatic curves for LiF[17] and Al,[19].[20]

Figure 6. Dependencies of α on T_e in LiF crystal: i - ionic crystal and optical phonons, c - covalent crystal with excitation of optical and acoustical modes, a - wide-range approximation of α. Ionization degree $Z(T_e)$ in ionization equilibrium is also shown by the curve "Z".
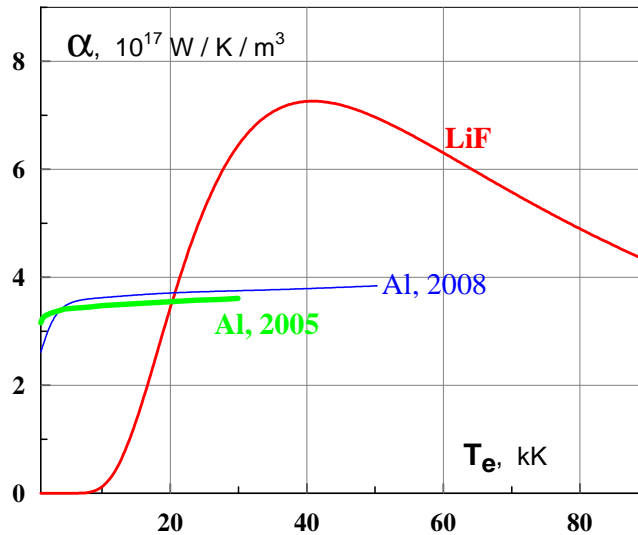
Figure 7. Comparison of coefficient α for dielectric and metal. There is an obvious difference in α (α gives power transfer per unit of volume) at small temperatures connected with small values of Z in dielectrics. Wide-range approximation "LiF" is taken from Fig. 6. Dependencies for Al are from[22] "Al, 2005" and from[23, 24] "Al, 2008".

5. ELECTRON-ION ENERGY EXCHANGE

Theory of electron-phonon interaction in LiF crystal gives results shown in Figs. 6 and 7. In LiF, calculations have been done taking into account that this ionic crystal tends to be covalent type crystal with increase of concentration n_e of free carriers. Strong polariton interaction mainly with light Li^+ ion increases α fast with increase of concentration of free electrons. This is clear from the curve "i" in Fig. 6. But at large n_e concentrations an ionic crystal transforms to a configuration similar to a covalent crystal since positive excess of electron charge of F^- ion gradually disappears as number of electrons lifted from valent band increases. This process saturates growth of α, see the curve "c" in Fig. 6. The approximation "a" from Fig. 6 has been used in the computer simulations of system n_e, T_e, T_i-hd (1-6).
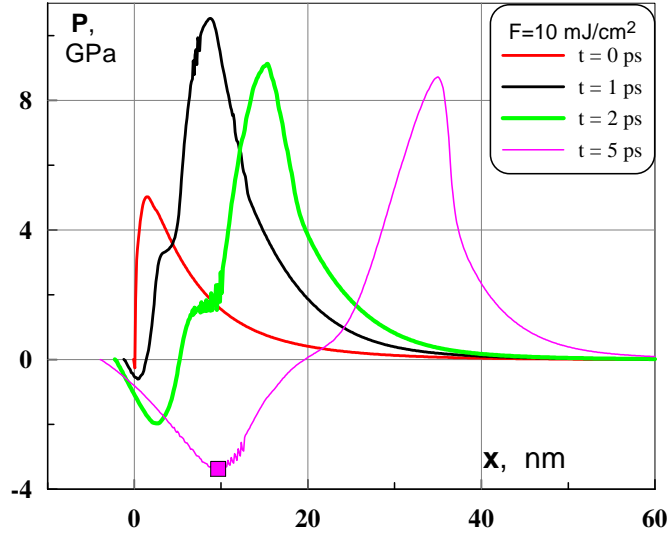
Figure 8. Formation of compression wave after action of EUV-FEL pulse in the ablation near-threshold regime with $\tau_L = 300\text{fs}$ and fluence $F = 10\text{mJ/cm}^2$. The square marker in the pressure profile for $t = 5\text{ps}$ gives position $(t, x, \text{or } x^0)$ and absolute value of the maximum instant negative pressure $|p_{neg}(t = 5\text{ps})|_{max}$.

In the ionic crystal electrons interact with the longitudinal optical vibrations of ions due to the strong electric field created by these vibrations. When electrons are excited into the conduction band, pure ionic character of a crystal changes because of the appearance of neutral Fluorum atoms. It is equivalent to the change of some ionic type bonds between atoms into the covalent bonds and pure metal bonds. That is why when the number of electrons in the conduction band increases, it increases the importance of the interactions of electrons with the acoustical phonons and decreases the importance of the interactions of electrons with the optical phonons. Our calculated electron-phonon coupling factor α takes into account interaction of electrons in the conduction band both with optical and acoustical longitudinal phonons.

Coefficients α shown as the curves "i" and "c" in Fig. 6 and the curve "Al, 2005"[22] in Fig. 7 were calculated with taking into account Thomas-Fermi screening of Coulomb interaction without the use of any adjustable parameters. The curve "Al, 2008" in Fig. 7 has been calculated in.[23] This calculation uses Eliashberg spectral function and adjustable parameter λ.[25, 26] It should be mentioned that very different approaches[22] and[23] give similar results for the coefficient α of Al, see Fig. 7.

6. DYNAMICS OF HEATING AND EXPANSION OF LIF CRYSTAL

Model n_e, T_e, T_i-hd (1-6) with parameters described in Sections 4 and 5 has been used to simulate action of EUV-FEL onto LiF dielectric. Experimental results concerning EUV-FEL/LiF have been presented in Section 2. Formation and propagation of shock after EUV-FEL action are shown in Figs. 8-10. Parameters are typical for experiments. They are: pulse duration $\tau_L = 300\text{fs}$, photon energy 20.2 eV, $D_{att} = 9\text{nm}$. Heat penetration depth is smaller than in case of metals[15, 20, 27] since the stage of supersonic propagation of electron heat wave[28] is absent in dielectrics (while a skin-depth for OL and metals is comparable with D_{att}). Therefore the shock wave in LiF appears earlier than in metal.

At instant $t = 0$ half of fluence is delivered, see (7). Maximum of total pressure $p = p_i + p_e$ is achieved slightly later after the end of a heating laser pulse. Because, firstly, two-temperature relaxation lasts longer than $\tau_L = 300\text{fs}$, and, secondly, electronic gas is softer than condensed matter (at equal internal energies of electron and ion subsystems pressure p_e is smaller than p_i). After propagation through some distance, the compression wave breaks due to its non-linearity and forms a pressure jump (shock wave). The more non-linear is the wave (larger F, p), the faster it breaks. Shock decays during its subsequent propagation into bulk, see Figs. 9 and 10. Shock attenuation is faster for more non-linear shock. This attenuation is connected with rarefaction wave coming to the shock from the vacuum boundary side.
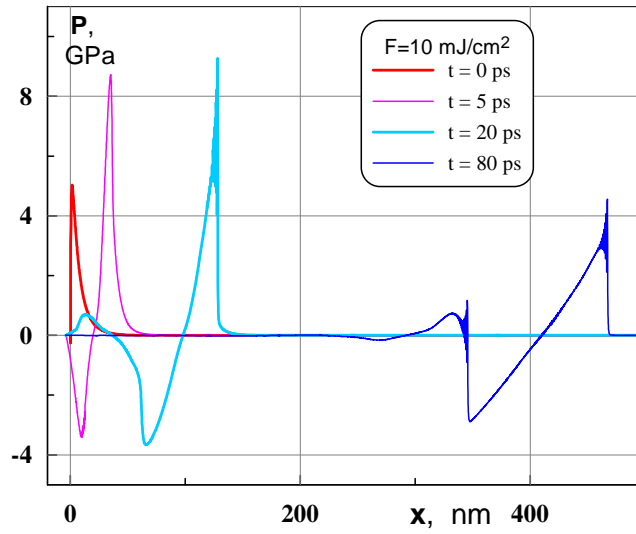
Figure 9. Appearance of shock as a result of breaking of compression wave, $\tau_L = 300\text{fs}$, $F = 10\text{mJ/cm}^2$. Let us mention that two shocks appear: one before the compression wave, while other behind the stretching wave. There is also appearance of second compression $p > 0$ and second stretching $p < 0$ behind main "plus and minus" acoustic pulse, compare with paper.[20]
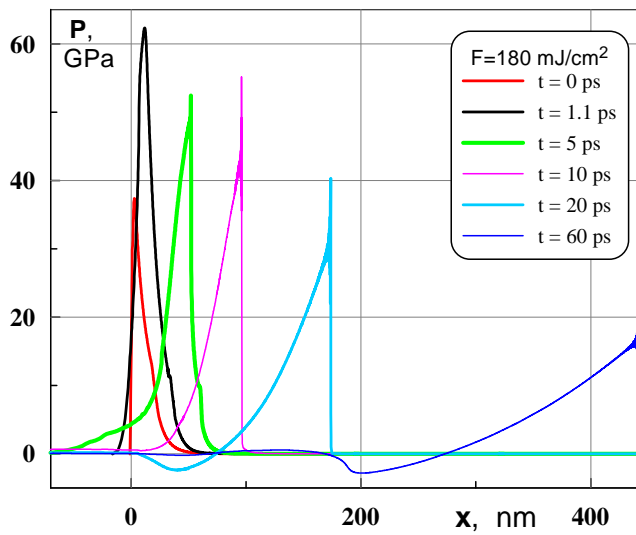

Figure 10. Formation of powerful acoustic disturbance after action of strong EUV-FEL pulse, $\tau_L = 300\text{fs}$, $F = 180\text{mJ/cm}^2$.
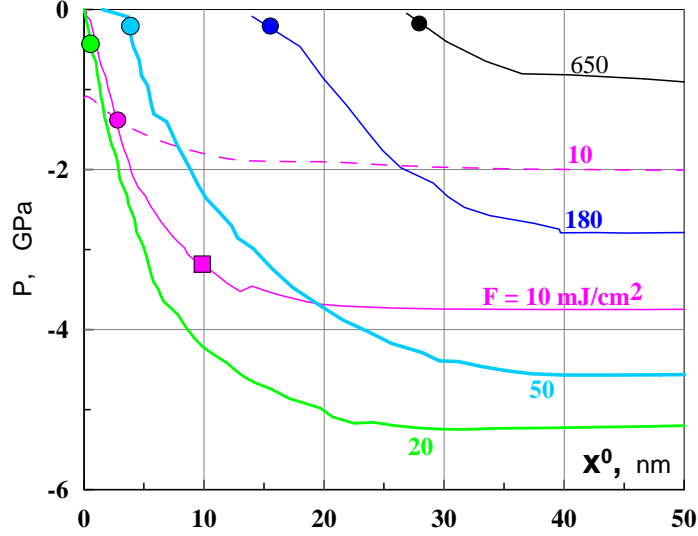
Figure 11. The continuous curves give dependencies $|p_{neg}|_{max}$ on Lagrangian coordinate x^0. The square marker in profile $F = 10\text{mJ/cm}^2$ corresponds to the apex point of the well in Fig. 8 marked by the same marker. Its coordinates are: $t = 5\text{ps}$, $|p_{neg}|_{max} = 3.4\text{GPa}$, $x = 10\text{nm}$, $x^0 = 9.7\text{nm}$. The difference between x and x^0 is die to motion of substance. The dashed curve presents material strength p_{lim} for the case $F = 10\text{mJ/cm}^2$. Fluencies are written as digits near curves.

Near threshold fluence $F_{abl} \approx 10\text{mJ/cm}^2$ the maximum electron temperature is $T_e \approx 20\text{kK}$, the maximum ionization degree is near 3%. Two-temperature relaxation lasts $t_{eq} \sim 1\text{ps}$. Maximum T_i is 1.5 kK. The values for fluence $F = 180\text{mJ/cm}^2$ are: $T_e|_{max} \approx 110\text{kK}$, $Z|_{max} \approx 0.4 - 0.5$ (in the dense part of LiF where $\rho \approx 2.6\text{g/cc}$ near the end of two-temperature relaxation), $T_i|_{max} \approx 10\text{kK}$, $t_{eq} \approx 1 - 2\text{ps}$. Fluence $F \approx 180\text{mJ/cm}^2$ is the highest fluence achieved in EUV-FEL experiments presented in Section 2.

Low fluence $F \sim F_{abl}$ and high fluence $F \sim 200\text{mJ/cm}^2$ EUV-FEL pulses produce different negative pressures profiles which are responsible for spallative ablation at low fluence. This mechanism of ablation has been proposed for explanation of very low values of ablation threshold in case of XRL.[2] In work[2] only the near-threshold case for Ag XRL has been considered experimentally and theoretically. Here we study ablation in wide range of fluencies.

From Figs. 8-11 we see that in the near-threshold case, negative pressure is achieved in early stages, at shallow depth $\approx 10\text{nm}$, and its amplitude $|p_{neg}| \approx 3.5\text{GPa}$ is approximately half of the amplitude of compression wave. At large fluencies, the situation is different. Negative pressures appear later, and at significant depths, their maximum amplitude $|p_{neg}|_{max}$ is of the same order as in the near-threshold case. But now this amplitude is negligible part (less then 0.1 for $F = 180\text{mJ/cm}^2$) of the maximum compression pressure.

The dependencies $|p_{neg}|_{max}(x^0)$ in Fig. 11 show how the maximum tensile stress $|p_{neg}|_{max}$ evolves in space and time as the pressure waves presented in Figs. 8-10 penetrate into the LiF target. The square markers in Figs. 8 and 11 help to understand the sense of dependencies in Fig. 11. As was said in Section 4 we use EOS of Al[17,18] in computer simulation. In this case the maximum cold negative pressure $p_{neg}|_{max}(T = 0)$ is $\approx 12\text{GPa}$ according to paper[20] and References in it. In simulations (Figs. 8-11) we did not use technique which allows to include kinetics of nucleation (this will need another paper). In this case fragmentation is achieved when the system touches the spinodal. Simulations show that in our calculations, presented in 8-11, in cold part of our target the value of tensile stress near $p_{neg}|_{max}(T = 0)$ for Al is not achievable in the range of considered fluencies. Therefore we did not see separation of rather cold spallation plate from the rest of a target as it was in the paper.[20] But we see evaporation and fragmentation of rather hot matter from a thin surface layer when fluence F is large. This means that in our simulations the system touches the hot part of the spinodal (the spinodal ends in the critical point) and can not achieve the cold part of the spinodal which ends in the point $p_{neg}|_{max}(T = 0)$.
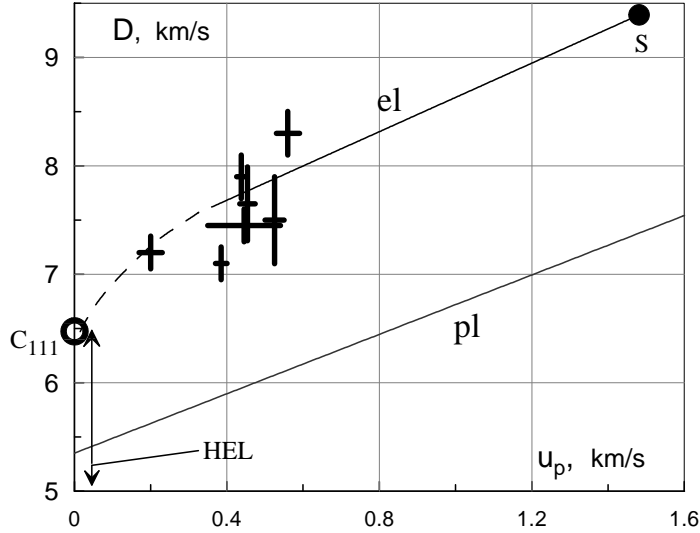
Figure 12. The shock adiabatic curves from laser experiment (crosses), from MD calculations (the dependence "el"), and from the works[17,18] ("pl"). The curves "el" and "pl" correspond to elastic and plastic states. We see that crosses are near the curve "el". This proves that Al crystal is elastic behind very strong shocks.

We estimate thickness of rather cold spallation plate in the following way. Firstly, the material strength (or limiting stress) $p_{lim}(T)$ is found. Secondly, values of $|p_{neg}|_{max}(x^0)$ in simulations are compared with $p_{lim}(T)$. The dashed curve in Fig. 11 gives the profile of material strength $p_{lim}(x^0)$ in substance heated by EUV-FEL pulse. Dependence $p_{lim}(T)$ has been taken as 30%-60% value of material strength for Al known at high deformation rate from the paper.[27] In Fig. 11 the intermediate dependence $p_{lim}(T)[\text{GPa}] = -2.2 + 0.7T[\text{kK}]$ is shown as the dashed curve. A temperature profile $T(x)$ has been taken from simulation and has been substituted into the function $p_{lim}[T(x^0)]$. The intersection point of the curves $p_{lim}(x^0)$ and $|p_{neg}|_{max}(x^0)$ is denoted by the circle marker in Fig. 11 for the case with $F = 10\text{mJ/cm}^2$. Intersections at the different fluencies F are denoted by the different circle markers.

7. ABLATION BY OPTICAL LASERS

Action of OL onto Al-film is considered in[27] (Al is aluminum). The Al-film is deposited onto glass plate. Pump OL pulse comes through glass and illuminates boundary between glass and Al. Molecular dynamics (MD) simulation of this laser experiment shows that Al crystal remains in elastic state even at very high shear stress p_{sh}. Usually it is supposed that crystal transforms into plastic state when the stress p_{sh} overcomes threshold value p_{sh}^{lim} which is of the order of 1% of the shear modulus G; for Al $G \approx 26$ GPa (wikipedia). In our laser experiment[27] crystal keeps its elasticity at shear amplitudes p_{sh} order of magnitude higher than the value of one percent from the modulus G.

Experimental data from[27] allows us to plot a shock adiabatic curve of Al crystal in the laser experiment. It is presented in usual variables u_p, D, where u_p is piston velocity, D is shock velocity, both in laboratory frame. In this frame matter before the shock is at rest. Piston moving with constant velocity u_p supports a shock moving with velocity D. The experimental shock adiabatic curve is shown by the crosses in Fig. 12. The sizes of the crosses are defined by errors in measurements.

Here we presents new results of MD simulations of shock propagation in initially homogeneous fcc Al crystal along direction 111. The shock is supported by piston moving with constant velocity u_p. The results of the MD simulations are shown as the continuous straight line "el" in Fig. 12. They are obtained by varying of velocity u_p in the set of the simulations. The dashed extension of the continuous line "el" in Fig. 12 smoothly connects the last simulated point of the continuous line "el" and the point C_{111}. The value $C_{111} = 6.473$ km/s for longitudinal sound velocity along direction 111 is taken from the reference book. Abbreviation "HEL" in Fig. 12 is used for

the usually used value of Hugoniot Elastic Limit. It corresponds to the threshold shear $p_{sh}^{lim} \sim 1\%$ of the modulus G.

The crystal behind the shock "el" is in elastic metastable state relative to nucleation of dislocation loops. Nucleation of loops triggers transformation from elastic to plastic state. The laser loading is so fast that loops have no time to appear. The point S in Fig. 12 limits the shock adiabatic curve "el" from the high pressures side. It corresponds to the spinodal where the amplitude of shear stress is so high that matter behind shock transforms into plastic state at an atomic time scale.

The experimental crosses are near the elastic adiabatic curve, see Fig. 12. The elastic and plastic curves differ significantly. Experimental errors are less than this difference.

This means that for the first time it is proved that very high amplitude elastic shocks exist in nature. The proof is based on combination of experimental measurements and numerical modeling.

ACKNOWLEDGMENTS

REFERENCES

1. A. Ya. Faenov, N. A. Inogamov, V. V. Zhakhovskii, V. A. Khokhlov, K. Nishihara, Y. Kato, M. Tanaka, T. A. Pikuz, M. Kishimoto, M. Ishino, M. Nishikino, T. Nakamura, Y. Fukuda, S. V. Bulanov, and T. Kawachi, "Low-threshold ablation of dielectrics irradiated by picosecond soft x-ray laser pulses," *Applied Physics Letters* **94**, p. 231107, 2009.

2. N. A. Inogamov, A. Ya. Faenov, V. A. Khokhlov, V. V. Zhakhovskii, Yu. V. Petrov, I. Yu. Skobelev, K. Nishihara, Y. Kato, M. Tanaka, T. Pikuz, M. Kishimoto, M. Ishino, M. Nishikino, Y. Fukuda, S. V. Bulanov, T. Kawachi, S. I. Anisimov, and V. E. Fortov, "Spallative ablation of metals and dielectrics," *Contrib. Plasma Phys.* **49**, p. 455, 2009.

3. M. Nishikino, N. Hasegawa, T. Kawachi, H. Yamatani, K. Sukegawa, and K. Nagashima, "Characterization of a high-brillance soft x-ray laser at 13.9 nm by use of an oscillator-amplifier configuration," *Applied Optics* **47**, p. 1129, 2008.

4. Y. Ochi, N. Hasegawa, T. Kawachi, and K. Nagashima, "Development of a chirped pulse amplification laser with zigzag slab Nd:glass amplifiers dedicated to x-ray laser research," *Applied Optics* **46**, p. 1500, 2007.

5. T. Inagaki, S. Imoue, M. Ishi, Y. Kim, H. Kimura, M. Kitamura, T. Kobayashi, H. Maesaka, T. Masuda, S. Matsui, T. Matsushita, X. Marechal, M. Nagasono, H. Ohashi, T. Ohata, T. Ohshima, K. Onoe, K. Shirasawa, T. Takagi, S. Takahashi, M. Takeuchi, K. Tamasaku, R. Tanaka, Y. Tanaka, T. Tanikawa, T. Togashi, S. Wu, A. Yamashita, K. Yanagida, C. Zhang, H. Kitamura, and T. Ishikawa, "A compact free-electron laser for generating coherent radiation in the extreme ultraviolet region," *Nature Photonics* **2**, p. 555, 2008.

6. T. Shintake, H. Tanaka, T. Hara, T. Tanaka, K. Togawa, M. Yabashi, Y. Otake, Y. Asano, T. Fukui, T. Hasegawa, A. Higashiya, N. Hosoda, T. Inagaki, S. Inoue, Y. Kim, M. Kitamura, N. Kumagai, H. Maesaka, S. Matsui, M. Nagasono, T. Ohshima, T. Sakurai, K. Tamasaku, Y. Tanaka, T. Tanikawa, T. Togashi, S. Wu, H. Kitamura, T. Ishikawa, T. Asaka, T. Bizen, S. Goto, T. Hirono, M. Ishii, H. Kimura, T. Kobayashi, T. Masuda, T. Matsushita, X. Marechal, H. Ohashi, T. Ohata, K. Shirasawa, T. Takagi, S. Takahashi, M. Takeuchi, R. Tanaka, A. Yamashita, K. Yanagida, and C. Zhang, "Stable operation of a self-amplified spontaneous-emission free-electron laser in the extremely ultraviolet region," *Physical Review Special Topics - Accelerators and Beams* **12**, p. 070701, 2009.

7. M. Kato, N. Saito, T. Tanaka, Y. Morishita, H. Kimura, H. Ohashi, M. Nagasono, M. Yabashi, K. Tono, T. Togashi, A. Higashiya, and T. Ishikawa, "Pulse energy of the extreme-ultraviolet free-electron laser at SPring-8 determined using a cryogenic radiometer," *Nuclear Instruments and Methods in Physics Research A* **612**, p. 209, 2009.

8. G. Baldacchini, S. Bollanti, F. Bonfigli, P. Di. Lazzaro, A. Ya. Faenov, F. Flora, T. Marolo, R. M. Montereali, D. Murra, E. Nichelatti, T. Pikuz, A. Reale, L. Reale, A. Ritucci, and G. Tomassetti, "Point defects in lithium fluoride by EUV and soft X-rays exposure for X-ray microscopy and optical applications," *IEEE Journal of Selected Topics in Quantum Electronics* **10**, p. 1435, 2004.

9. G. Baldacchini, S. Bollanti, F. Bonfigli, F. Flora, P. Di. Lazzaro, A. Lai, T. Marolo, R. M. Montereali, D. Murra, A. Faenov, T. Pikuz, E. Nichelatti, G. Tomassetti, A. Reale, L. Reale, A. Ritucci, T. Limongi, L. Palladino, M. Francucci, S. Martellucci, and G. Petrocelli, "Soft x-ray submicron imaging detector based on point defects in LiF," *Rev. Sci. Instrum.* **76**, p. 113104, 2005.

10. G. Tomassetti, A. Ritucci, A. Reale, L. Palladino, L. Reale, L. Arrizza, G. Baldacchini, F. Bonfigli, F. Flora, L. Mezi, R. M. Montereali, S. V. Kukhlevsky, A. Faenov, T. Pikuz, and J. Kaiser, "High-resolution imaging of a soft-X-ray laser beam by color centers excitation in lithium fluoride crystals," *Europhys. Lett.* **63**, p. 681, 2003.

11. A. Ya. Faenov, Y. Kato, M. Tanaka, T. A. Pikuz, M. Kishimoto, M. Ishino, M. Nishikino, Y. Fukuda, S. V. Bulanov, and T. Kawachi, "Submicrometer-resolution in situ imaging of the focus pattern of a soft x-ray laser by color center formation in LiF crystal," *Optics Letters* **34**, p. 941, 2009.

12. Y. Fukuda, A. Ya. Faenov, T. Pikuz, M. Kando, H. Kotaki, I. Daito, J. Ma, L. M. Chen, T. Homma, K. Kawase, T. Kameshima, T. Kawachi, H. Daido, T. Kimura, T. Tajima, Y. Kato, and S. V. Bulanov, "Soft X-ray source for nanostructure imaging using femtosecond-laser-irradiated clusters," *Appl. Phys. Lett.* **92**, p. 121110, 2008.

13. Y. Ochi, T. Kawachi, N. Hasegawa, M. Nishikino, T. Ohba, M. Tanaka, M. Kishimoto, T. Kaihori, K. Nagashima, and A. Sugiyama, "Demonstration of submicrojoule, spatially coherent soft-x-ray laser pumped by 0.1 hertz, 10 joule, picosecond laser," *Japanese Journal of Applied Physics* **48**, p. 120212, 2009.

14. E. D. Palik. (Ed.), *Handbook of Optical Constants of Solids*, Academic Press, New York, 1998.

15. N. A. Inogamov, V. V. Zhakhovskii, S. I. Ashitkov, V. A. Khokhlov, Yu. V. Petrov, P. S. Komarov, M. B. Agranat, S. I. Anisimov, and K. Nishihara, "Two-temperature relaxation and melting after absorption of femtosecond laser pulse," *Applied Surface Science* **255**, p. 9712, 2009.

16. L. D. Landau and E. M. Lifshitz, *Statistical Physics*, Butterworth-Heinemann, Oxford, 1986.

17. Shock wave database: http://teos.ficp.ac.ru/rusbank/.

18. A. V. Bushman, G. I. Kanel', A. L. Ni, and V. E. Fortov, *Intense dynamic loading of condensed matter*, Taylor & Francis, 1993.

19. J. H. Rose, J. R. Smith, F. Guinea, and J. Ferrante, "Universal features of the equation of state of metals," *Phys. Rev. B* **29**, p. 2963, 1984.

20. V. V. Zhakhovskii, N. A. Inogamov, Yu. V. Petrov, S. I. Ashitkov, and K. Nishihara, "Molecular dynamics simulation of femtosecond ablation and spallation with different interatomic potentials," *Applied Surface Science* **255**, p. 9592, 2009.

21. I. I. Sobelman, L. A. Vainshtein, and E. A. Yukov, *Excitation of Atoms and Broadening of Spectral Lines*, Springer Series on Atoms and Plasma, Springer, 2007.

22. Yu. V. Petrov, "Energy exchange between the lattice and electrons in a metal under femtosecond laser irradiation," *Laser and Particle Beams* **23**, pp. 283–289, 2005.

23. Z. Lin, L. V. Zhigilei, and V. Celli, "Electron-phonon coupling and electron heat capacity of metals under conditions of strong electron-phonon nonequilibrium," *Phys. Rev. B* **77**, p. 075133, 2008.

24. http://www.faculty.virginia.edu/CompMat/electron-phonon-coupling/.

25. P. B. Allen, "Theory of thermal relaxation of electrons in metals," *Phys. Rev. Lett.* **59**, p. 1460, 1987.

26. X. Y. Wang, D. M. Riffe, Y. S. Lee, and M. C. Downer, "Time-resolved electron-temperature measurement in a highly excited gold target using femtosecond thermionic emission," *Phys. Rev. B* **50**, p. 8016, 1994.

27. M. B. Agranat, S. I. Anisimov, S. I. Ashitkov, V. V. Zhakhovskii, N. A. Inogamov, P. S. Komarov, A. V. Ovchinnikov, V. E. Fortov, V. A. Khokhlov, and V. V. Shepelev, "Strength properties of an aluminum melt at extremely high tension rates under the action of femtosecond laser pulses," *JETP Letters* **91**, pp. 471–477, 2010.

28. N. A. Inogamov and Yu. V. Petrov, "Thermal conductivity of metals with hot electrons," *Journal of Experimental and Theoretical Physics* **110**, pp. 446–468, 2010.